

Nanostructured Ionic Liquid Containing Block Copolymer Electrolytes for Solid-State Supercapacitors

Anto Puthussery Varghese,^[a, b] Daniela de Morais Zanata,^[b, c] Sima Lashkari,^[b] Miryam Criado-González,^[b] Maria Forsyth,^[a, d] Patrick C. Howlett,^[a] Andrew N. Rider,^[e] Nicolas Goujon,^{*[b, c]} and Irune Villaluenga^{*[b, d]}

We report on the physiochemical behaviour of membranes based on three different polystyrene-*b*-poly(ethylene oxide)-*b*-polystyrene (PS-*b*-PEO-*b*-PS) block copolymers and an ionic liquid (1-ethyl-3-methylimidazolium bis(trifluoromethylsulfonyl)imide (EMIMTSI)) and their use as solid-state electrolytes in supercapacitors. The nanostructured block copolymers form free standing membranes at high ionic liquid uptake with conductivities above 1 mS/cm at 25 °C, keeping ordered morphologies. We used small angle X-ray scattering (SAXS) to propose the correlation between domain spacing, the copolymer chain length (*N*) and the interaction parameter (χ_{eff}) in the block copolymers. We explored the potential of the electrolytes in two high voltage (3.0 V) device

configurations, first using carbon nanotube (CNT) electrodes, with excellent electrical conductivity and high-rate capability exhibiting a power density of 5.7 KW/kg at 4 A/g, while devices based on high surface area activated carbon exhibited high energy density of 20.7 Wh/kg at 4 A/g. Overall, both devices deliver superior specific energy and power densities than that of commercial state-of-the-art supercapacitors, based on liquid electrolyte. Additionally, the CNT|Solid-state|CNT device displays higher power density compared to the AC|Solid-state|AC device, highlighting its better suitability for high power applications, while the AC|Solid-state|AC device, is better suited for energy density applications.

Introduction

Rapid adoption of clean energy sources and increasing awareness towards climate change has cemented the needed for efficient energy storage technologies. Electrochemical double layer capacitors (EDLC) or supercapacitors play a major role in fulfilling the emerging energy storage demands of

integrated systems.^[1] Supercapacitors are characterized by their high-power density and are used in applications requiring burst power delivery, hybrid vehicles, military, and space applications.^[2] EDLC devices store energy via the accumulation of ions at electrode/electrolyte interface and therefore cycle life of such devices far exceeds that of batteries over millions of cycles. Commercially, carbon-based materials are preferred in the electrode structures owing to their high surface area leading to higher energy and power densities.^[3] Materials such as activated carbon (AC), carbon fibres (CF) and carbon nanotubes (CNTs) are all used to enhance electrochemical performance of supercapacitors.^[4,5] CNTs are attractive materials due to the sp^2 graphitic carbon structure and excellent electrical conductivity for applications requiring device flexibility.^[6] The capacitance of an EDLC electrode is influenced by several factors including the surface area, morphology, electrical conductivity, and the electrolyte used. Whilst there are a plethora of reports on aqueous based systems where the working voltage is limited by the breakdown potential of water,^[6–10] the potential of high voltage electrolytes remains relatively unexplored. In this aspect ionic liquids (ILs) hold tremendous potential^[11–13] as eco-friendly materials, possessing low vapour pressure, high thermal and chemical stability and with a wide electrochemical stability window, unlike aqueous or organic electrolytes.^[14–18] However, electrolyte leakage, corrosion, and packaging problems are still issues to be resolved. To overcome these challenges, solid electrolytes composed of a polymer matrix and ionic liquids have been developed,^[14,16–18] although a good balance between ionic conductivity and mechanical performance is still challenging in solid electrolytes. As such, block copolymers are very promising candidates to be

- [a] A. P. Varghese, M. Forsyth, P. C. Howlett
Institute for Frontier Materials (IFM) and ARC Industry Training Transformation Centre for Future Energy Technologies (storEnergy), Deakin University, 221 Burwood Highway, Victoria, 3125, Australia
- [b] A. P. Varghese, D. M. Zanata, S. Lashkari, M. Criado-González, N. Goujon, I. Villaluenga
POLYMAT, Applied Chemistry Department, Faculty of Chemistry, University of the Basque Country UPV/EHU, Donostia San Sebastián, Spain
E-mail: ngoujon@cicernergigune.com
irune.villaluenga@polymat.eu
- [c] D. M. Zanata, N. Goujon
Center for Cooperative Research on Alternative Energies (CIC EnergigUNE), Basque Research and Technology Alliance (BRTA), Parque Tecnológico de Alava, Albert Einstein 48, 01510 Vitoria-Gasteiz, Spain
- [d] M. Forsyth, I. Villaluenga
Ikerbasque, Basque Foundation for Science, 48013 Bilbao, Spain
- [e] A. N. Rider
Multifunctional Materials Group, Defence Science and Technology Group, Port Melbourne, 3207, Australia
-  Supporting information for this article is available on the WWW under <https://doi.org/10.1002/batt.202400591>
-  © 2024 The Author(s). *Batteries & Supercaps* published by Wiley-VCH GmbH. This is an open access article under the terms of the Creative Commons Attribution Non-Commercial NoDerivs License, which permits use and distribution in any medium, provided the original work is properly cited, the use is non-commercial and no modifications or adaptations are made.

used as the polymer matrix. Block copolymers based on poly(ethylene oxide) (PEO) covalently bonded to a rigid polystyrene (PS) have been proven to be particularly versatile due to their well-established self-assembly. Moreover, the introduction of a non-conductive domain inaccessible to the IL tremendously improves the physicochemical properties of the system. Block copolymers exhibit a phase separated and controlled morphology, which highly depends on the volume fractions of the conducting and non-conducting phases.^[19] The addition of ionic liquids to such block copolymers, which is necessary to imbue them with ionic conductivity for EDLC applications, can have a significant impact on the material properties. Therefore, in order to design optimum electrolytes for supercapacitors, it is essential to study and understand the effect of the ionic liquid on block copolymers. Here, we have developed nanostructured block copolymer electrolytes with high ionic liquid uptake. The effect of the ionic liquid (1-ethyl-3-methylimidazolium bis(trifluoromethylsulfonyl)imide (EMIMTS-Fl)) on electrochemical, morphological, thermal and mechanical properties of triblock copolymers (PS-*b*-PEO-*b*-PS (SEOS)) was studied. Finally, we test the optimum electrolyte in two high voltage device configurations.

Experimental Section

Materials

4-Cyano-4-(dodecylsulfanylthiocarbonyl)sulfanylpentanoic acid (CDTPA, 97%, abcr), N,N'-Dicyclohexylcarbodiimide (DCC, 99%, Thermo Scientific), 4-(dimethylamino)pyridine (DMAP, 99%, Thermo Scientific), anhydrous dichloromethane (DCM, 99.8%, Acros), diethyl ether (99%, Thermo Scientific) and dimethylformamide (DMF, 99.5%, Acros) were used as received. 2,2'-Azobis(2-methylpropionitrile) (AIBN, initiator, 98%, Aldrich) was purified by recrystallization from methanol. Poly(ethylene oxide) (PEO, Mw 35000 g mol⁻¹, Aldrich) was dried at 90°C under a high vacuum for 20 h. Styrene (sty, 99%, Aldrich) was passed through an alumina column. 1-ethyl-3-methylimidazolium bis(trifluoromethylsulfonyl)imide (EMIM TFSI) was purchased from Solvionic with 99.9% purity and further dried under vacuum on a Schlenk line (i.e., a vacuum gas manifold) at 50°C to remove traces of moisture. The ionic liquid was stored in an Argon filled glovebox. CNT mat was purchased from Huntsman, USA as MIRALON® sheet and used as structural supercapacitor electrodes without any surface modifications.

Synthesis of PEO-macroCTA

PEO-macroCTA was synthesized following a similar procedure described

by Porcarelli *et al.*^[20] using the following quantities of reactants: PEO (10 g, 0.29 mol) CDTPA (1.38 g, 3.4 mmol), DCC (0.77 g, 3.76 mmol) and DMAP (0.13 g, 1 mmol). Yield: 8.0 g (80%).

NMR (300 MHz, δ ppm, CDCl₃): 3.6 (3180 H, -COOCH₂CH₂OCH₂CH₂O-), 3.3 (4H, 2 S-CH₂), 2.3–2.7 (8H, 2 CH₃-(CN)-S-C-(CH₂)), 1.9 (6 H, 2 SC(CN)-CH₃), 1.2–1.4 (40 H, CH₂), 0.9 (6H, 2 CH₃).

Synthesis of PS-*b*-PEO-*b*-PS (SEOS) Triblock Copolymers

An example is provided for the preparation of SEOS_0.7: a solution containing PEO-macroCTA (1.7 g, 0.05 mmol), styrene (2.7 g, 26 mmol), and DMF (5 mL) was placed in a Schlenk tube equipped with a magnetic stir bar. The reaction mixture was subjected to three freeze-pump-thaw cycles, flushed with argon, and placed into an oil bath pre-heated at 70°C. A solution of AIBN (2.5 mg, 0.015 mmol) in DMF (0.1 mL), previously degassed and flushed with argon, was added. The polymer purification was performed by precipitation in cold diethyl ether, followed by centrifugation and vacuum drying (50°C, 12 h). All SEOS copolymers were prepared similarly by changing the molar ratio between the initial concentration of the styrene monomer and the PEO macro-CTA. D_P _{PEO} and D_P _{PS} are the degrees of polymerization of the PEO (PEO) and polystyrene (PS), were determined by ¹H NMR^[21], respectively Figure 1.

The PS-*b*-PEO-*b*-PS triblock copolymers structure was confirmed by ¹H NMR spectroscopy, where the peaks associated with PS (δ=6.3–7.2 ppm) and PEO blocks (δ=3.65 ppm). The degrees of polymerization of PS blocks were calculated considering the molar fractions of PS and PEO (obtained by ¹H NMR) and the degree of polymerization of PEO. GPC curves showed the absence of unreacted PEO macroCTA in the SEOS block copolymers and their dispersity (D) presents satisfactory values, between 1.2 and 1.8 and is shown in Figure S1 and Table S1.

The chain length calculated as $N = (N_{PS} + N_{PEO})/2$, where

$$Ni = \frac{Mi}{\rho_i N_A V_{ref}} \quad (i = PS \text{ or } PEO) \quad (1)$$

Where N_A is the Avogadro number, V_{ref} was fixed as 0.1 nm,^[3] densities of PEO and PS at 25°C were calculated using the equations $\rho_{PEO} = 1.130 - 7.31 \times 10^{-4} \times T$ and $\rho_{PS} = 1.08665 - 6.19 \times 10^{-4} \times T + 1.36 \times 10^{-7} \times T$.^[22]

Table 1 represents the EO volume fraction (ϕ_{EO}), and number average molar mass (M_n) determined by ¹H NMR for PEO macroCTA and their respective PS-*b*-PEO-*b*-PS copolymers. The table also represents the calculated chain lengths for PS and PEO and segregation strength for the pristine block copolymers.

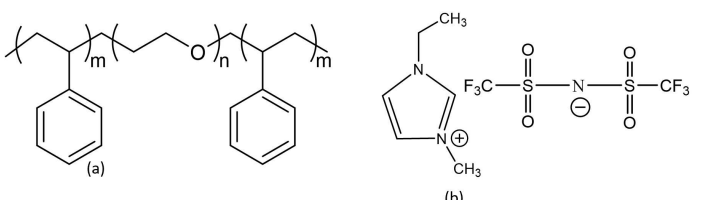


Figure 1. (a) Structure of PS-*b*-PEO-*b*-PS block copolymer, (b) EMIMTFSI ionic liquid.

Table 1. EO volume fraction and molecular weights as determined by ^1H NMR, chain length and segregation strength of the pristine block copolymers.							
Sample	ϕ_{EO}	^1H NMR (CDCl_3)					
		M_{PEO} (g/mol)	M_{PS} (g/mol)	M_{total} (g/mol)	N_{PS}	N_{PEO}	N_{Total}
PEO macroCTA	1	35000	—	35000	—	—	—
7SEOS	0.7	35000	12500	47500	194	518	356
6SEOS	0.6	35000	23500	58500	364	518	441
4SEOS	0.4	35000	38000	73000	589	518	554

Preparation of Polymer Electrolytes

The polymer electrolytes were prepared by solvent casting, EMIMTSFI was added per unit of ethylene oxide (EO) denoted by the r value, dissolved in tetrahydrofuran (THF). The resulting mixture was mechanically stirred for 1 h at 50 °C after which it was poured into Teflon moulds. The solvent was slowly evaporated overnight at room temperature and the as-formed film was first dried in a vacuum oven at 60 °C for 24 h. For preparation of the membranes, the iongel was further hot pressed between Teflon sheets at 110 °C resulting in membranes which were further dried in a Buchi vacuum oven at 80 °C overnight. The highest r value that was investigated was 0.45, as higher loadings of IL resulted in gels instead of self-standing membranes. The r values and corresponding volume fraction of conducting phase (EO + IL) in the polymer electrolytes are shown in Table 2.

The volume fraction of the conducting phase was calculated using Equation (2)^[22]

$$\Phi_c(r) = \frac{\nu_{EO} + r\nu_{EMIMTSFI}}{\nu_{EO} + r\nu_{EMIMTSFI} + \frac{M_{PS}M_{EO}}{M_s M_{PEO}} \nu_s} \quad (2)$$

Where ν_{EO} , $\nu_{EMIMTSFI}$ and ν_s are the molar volumes of ethylene oxide monomer units, 1-ethyl-3-methylimidazolium bis(trifluoromethylsulfonyl)imide and styrene monomer units, respectively, M_{EO} and M_s are the molar mass of ethylene oxide (44.05 g mol⁻¹) and styrene(104.15 g mol⁻¹), respectively. The calculated volume fractions of conducting phase are given in Table 2

Characterization Techniques

Nuclear Magnetic Resonance Spectroscopy (NMR)

^1H NMR spectra of the polymers were acquired in CDCl_3 (5 mg mL⁻¹), using a Bruker Avance 300 MHz spectrometer at 25 °C. The signal of the residual proton of the CDCl_3 ($\delta=7.26$ ppm) was used as the internal reference standard. Gel permeation chromatog-

raphy (GPC) was set up with a pump (LC-20 A; Shimadzu, Japan), an autosampler (Waters 717, Milford, MA), three columns in series (Styragel HR2, HR4, and HR6, with pore sizes ranging from 10² to 10⁶ Å) and a differential refractometer (Waters 2410, Milford, MA). The polymers were dissolved in GPC grade THF at a concentration of around 3 mg mL⁻¹ and filtered through a 0.45 mm polyamide filter. Chromatograms were obtained in THF (GPC grade) at 35 °C using a flow rate of 1 mL min⁻¹. Molecular weights were determined using a calibration curve based on polystyrene standards.

Ionic Conductivity

Ionic conductivity was measured using AC impedance spectroscopy using Autolab PGSTAT302 N (Metrohm) coupled to a Microcell HC temperature controller (rhd-instruments). The measurements were performed within a frequency range of 1 MHz to 100 mHz with an amplitude of 10 mV between 25 °C and 95 °C. The membrane was cut into 8 mm discs assembled in a TSC battery cell (rhd-instruments) in an argon filled glovebox.

Differential Scanning Calorimetry (DSC)

The measurements were completed using a Netzsch Differential Scanning Calorimetry (DSC) 214 (Polyma instrument). Prior to measurements, the samples were cooled to -100 °C and, following a 10 min temperature hold, the sample was heated to 100 °C at 10 °C min⁻¹ and held at 100 °C for 2 min.

Thermogravimetric Analysis (TGA)

Thermal stability of the polymer electrolytes was probed using a TGA Discovery (TA Instruments) under nitrogen atmosphere. The samples were heated form room temperature to 600 °C at a ramp rate of 10 °C min⁻¹.

Dynamic Mechanical Analysis (DMA)

DMA was performed on selected samples to analyse the mechanical performance of the membranes. The measurements used an ARES-G2 rheometer with a 10% strain between 25 °C and 180 °C and a rate of 5 °C min⁻¹.

Transmission Electron Microscopy (TEM)

Dark field STEM imaging of microtome cut membranes was performed at 200 kV on a Talos F200i field emission gun instrument equipped with a Bruker X-Flash100 XEDS spectrometer.

Table 2. r values and corresponding volume fraction of conducting phase in polymer electrolytes.

r (mol IL/mol EO)	Volume fraction of conducting phase ($\phi_{EO,IL}$)		
	7SEOS	6SEOS	4SEOS
0	0.70	0.60	0.40
0.07	0.77	0.66	0.54
0.17	0.84	0.74	0.63
0.3	0.88	0.80	0.70
0.45	0.91	0.84	0.76

Small Angle X-ray Scattering (SAXS)

SAXS was performed to study the morphology of the membranes at the ALBA Synchrotron Light facility in Barcelona. The measurements were performed on beamline BL11 – NCD-SWEET with a beam size of 130 μmx130 μm operating at 12.4 keV with SDD at 8 m. The samples were scanned for 60 frames with an exposure time of 1 s per frame. Polymer electrolytes were packed into aluminium pans in a glovebox and dried in the antechamber under vacuum at 50°C and closed post drying. The pan backgrounds were not subtracted as the contribution was negligible. The sam

Preparation of Symmetric Structural Supercapacitors and Electrochemical Characterisation

Two different symmetric cells were fabricated; one based on CNT mat (CNT|6SEOS_{0.45}|CNT) and a second one based on activated carbon using polymer electrolytes as binder (AC|6SEOS_{0.45}|AC). For the preparation of symmetric supercapacitors based on CNT mats (CNT|6SEOS_{0.45}|CNT), CNT mats of 8 mm diameter and solvent casted 6SEOS_{0.45} iongel of 12 mm diameter with a thickness of 220 microns were used as symmetric electrodes and electrolyte, respectively. The CNT mats were aligned on both sides of the SEOS membrane to form a symmetric supercapacitor and assembled as coin cells (CR2032) inside an argon filled glovebox. The coin cell was later heated to 85°C for 30 min in an oven, ensuring proper electrode/electrolyte contact was achieved before any measurements were carried out. For the preparation of electrodes based on activated carbon (AC|6SEOS_{0.45}|AC), the iongel 6SEOS_{0.45} was used as a binder with conductive carbon (C₆₅). The casting slurry was prepared using acetonitrile as solvent followed by mixing in a speed mixer. The resulting slurry was cast via doctor blading, dried in an oven at 60°C, followed by a second drying in a vacuum oven at 60°C. Symmetric cells were prepared by punching 8 mm discs and followed the procedure as in the case of CNT|6SEOS_{0.45}|CNT, except there was no heat treatment following cell assembly.

A biologic VMP3 electrochemical workstation was used to carry out all cyclic voltammetry (CV) experiments. In case of CNT|6SEOS_{0.45}|CNT cyclic voltammetry (CV) was performed at a scan rate of 50 mVs⁻¹. Separate CVs were performed on CNT electrodes in a voltage range from -0.1 V to -1.9 V and -1.1 V to 1.4 V in pure EMIM TFSI as the electrolyte, functioning as anode and cathode, respectively, in a standard three electrode cell. Galvanostatic charge-discharge (GCD) measurements of the supercapacitor were carried out using a Neware-battery testing system between a voltage range of 0.1 V to 3 V for the CNT|6SEOS_{0.45}|CNT configuration and 0.1 V to 2.8 V for the AC|6SEOS_{0.45}|AC configuration. Specific capacitance (Fg⁻¹) was calculated from the CV measurements using Equation (3).

$$C_{sp}(Fg^{-1}) = \frac{\int Idv}{(V \times m \times \Delta V)} \quad (3)$$

Where V was the scan rate (mVs⁻¹), m the mass in g, ΔV the potential window and t discharge time in seconds. Energy density (WhKg⁻¹) and power density (Wkg⁻¹) were calculated as per Equations (4) and (5).

$$E(W hKg^{-1}) = \frac{0.5 C_s V^2}{3.6} \quad (4)$$

$$P(W Kg^{-1}) = \frac{E \times 3600}{t} \quad (5)$$

Where C_s is the specific capacity (Fg⁻¹) and V is the voltage change during charge-discharge.

Specific capacitance was calculated from the GCD curves using Equation 6.

$$C_{sp} = \frac{I\Delta t}{Vm} \quad (6)$$

Where I is the discharge current, Δt the discharge time, V is the voltage drop, excluding the IR drop, and m, the mass of one electrode.

Results and Discussion

Ionic Conductivity

The dependence of the ionic conductivity, σ, of the block copolymer electrolytes with different volume fractions of the conductive phase (the ionic liquid is expected to be only located in PEO domains) at 25°C is shown in Figure 2a. The neat polymers 4SEOS, 6SEOS and 7SEOS have EO volume fractions of 0.4, 0.6 and 0.7 respectively. Upon the addition of ion liquid the resulting conductivity is clearly dependent on the volume fraction of the conductive phase. The ionic conductivity increases with the increase of the volume fraction for each block copolymer electrolyte. At same volume fractions of conducting phase (e.g. 0.84 for 7SEOS and 6SEOS), the ionic conductivities exhibited by the block copolymer electrolytes are different (8.1×10^{-4} S/cm and 2.1×10^{-3} S/cm for 7SEOS and 6SEOS, respectively). This difference in conductivity is due to the higher volume fraction of ionic liquid (0.24) in the 6SEOS block copolymer electrolyte compared to the volume fraction of the ionic liquid (0.14) in 7SEOS block copolymer electrolyte. Therefore, this indicates that neat block copolymers with a higher volume fraction of PEO requires a lower volume of ionic liquid to achieve similar conductivities. This is further evident in Figure 2b, which shows a plot of the ionic conductivity versus the ion content (r, as the ratio of IL to EO monomer units). At low r values, the ionic conductivity increases rapidly for 4SEOS and 6SEOS electrolytes (from 0.07 to 0.17 r values). However, the increase of the ionic conductivity (from 0.07 to 0.17 r values) for 7SEOS electrolyte is lower (from 3.3×10^{-4} S/cm to 8.1×10^{-4} S/cm). This fact indicates that at low r values (<0.1), the neat block copolymer with a high PEO volume fraction (≥ 0.7) are the best candidates to achieve high conductivities ($> 10^{-4}$ S/cm) at room temperature. For higher r values (>0.2), the three electrolytes present very similar ionic conductivities at 25°C, reaching the highest ionic conductivity at r=0.45 (2.0×10^{-4} S/cm, 2.1×10^{-4} S/cm, and 1.9×10^{-4} S/cm for 4SEOS, 6SEOS and 7SEOS electrolytes, respectively).

The dependence of the ionic conductivity of the block copolymer electrolytes, σ, on temperature at different r values is shown in Figure 3. The ionic conductivity increases with the increase of the temperature for all the three block copolymer electrolytes, regardless of the r value. At r=0.07, the highest conductivity is for the 7SEOS block copolymer electrolyte at all

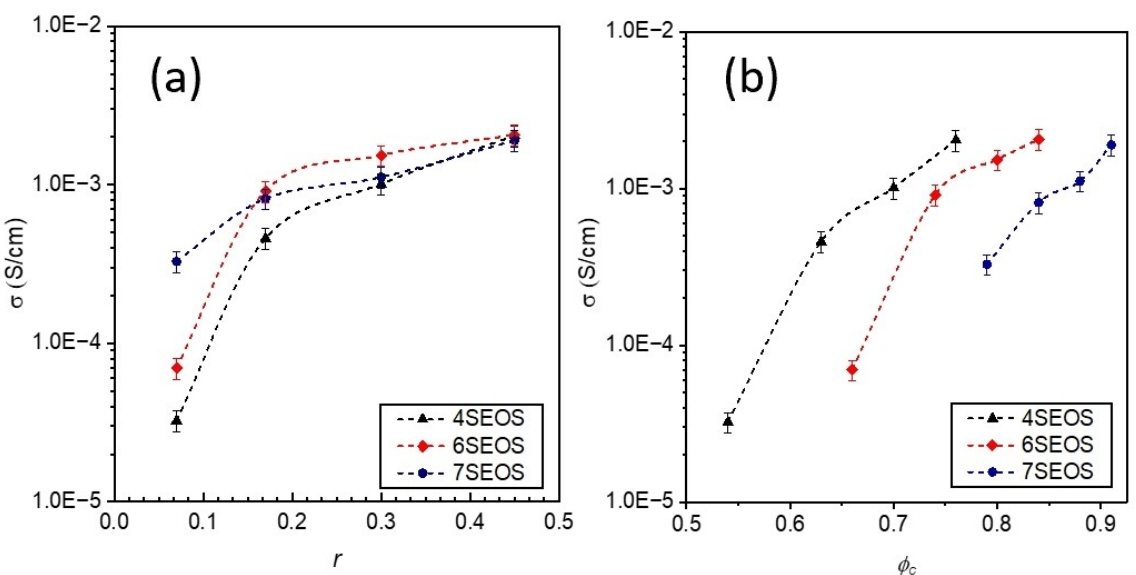


Figure 2. Ionic conductivity (σ) for the electrolytes at 25 °C (a) at different volume fractions of conducting phase (ϕ_c), and (b) at different r values.

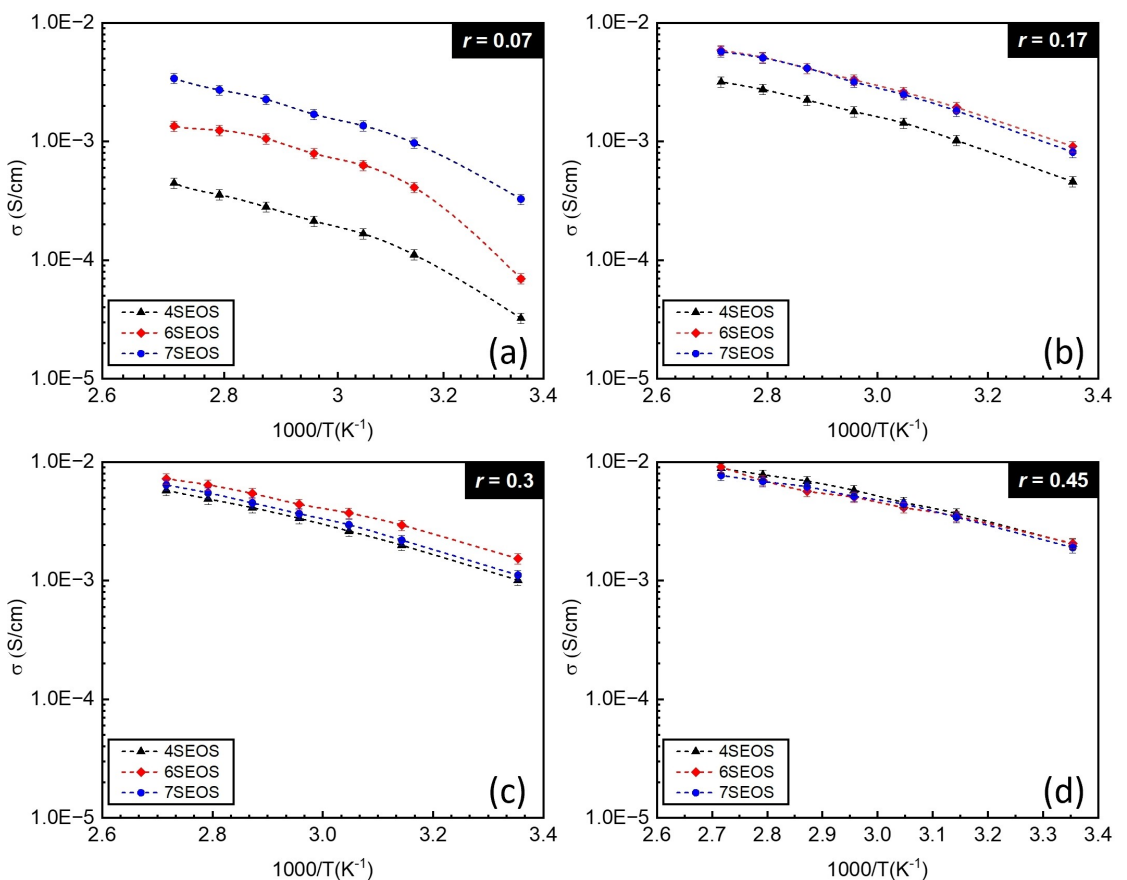


Figure 3. Ionic conductivity of polymer membranes as a function of r value for (a) $r = 0.07$, (b) $r = 0.17$, (c) $r = 0.3$, (d) $r = 0.45$.

temperature ranges. At $r = 0.17$, the highest conductivities are for 6SEOS and 7SEOS block copolymer electrolytes in all temperature ranges. At $r = 0.3$, the conductivity approaches similar values. At $r = 0.45$, the ionic conductivities are almost the same for the three block copolymer electrolytes over the whole

temperature range. This similar conductivity may be due to the relatively higher ionic liquid volumes, which could depress the T_g of the block copolymers, and consequently, increase the segmental motion of polymer chains.

DSC measurements of the block copolymer electrolytes at $r=0.45$, corresponding to the highest loading possible to form a free-standing film, were performed (Figure 4a). DSC traces for the neat PEO homopolymer are included for comparison. For the PEO homopolymer the glass transition temperature (T_g) is visible at -59°C with a clear melting peak (T_m) at 37°C . The T_g of the electrolytes at $r=0.45$ are observed at -71.4°C for 7SEOS and -69.0°C for both 6SEOS and 4SEOS, with no visible T_m , indicating the suppression of crystallinity. Therefore, T_g of the three block copolymer electrolytes are very similar, which is in good agreement with the obtained ionic conductivity results at $r=0.45$.

Figure 4b shows the thermal stability measurements for the block copolymer electrolytes at $r=0.45$. The electrolytes are stable up to 336°C for 7SEOS, and 352°C and 355°C for 6SEOS and 4SEOS, respectively. For each electrolyte, two distinct drops are observed corresponding to degradation of the block copolymer (PS-*b*-PEO-*b*-PS) and ionic liquid (EMIMTFSI), respectively. The weight loss associated with the first degradation is around 20 wt.% corresponding to the block copolymer at $r=0.45$. The second degradation event occurs at 420°C as EMIMTFSI begins to decompose, regardless of the electrolyte.

Consequently, the thermal stability of the three block copolymer electrolytes is compatible with any high temperature manufacturing processes such as those that may be required to produce structural supercapacitors.^[23]

SAXS profiles measured at 25°C for the 7SEOS, 6SEOS and 4SEOS electrolytes at different r values are shown in Figure 5. It is worth mentioning that 4SEOS at $r=0.45$ exhibited poor mechanical properties, which made the measurement problematic. All profiles contain a primary peak at $q=q^*$, indicating the presence of the periodic structures. However, broad scattering peaks are evidence of the lack of a long-range order, hindering the morphology identification. For 7SEOS block copolymer electrolyte, the order increases from $r=0$ to $r=0.07$. An order-disorder transition is observed from $r=0.07$ to $r=0.17$. Finally, the order increases from $r=0.17$ to $r=0.45$ for 7SEOS electrolyte. For 6SEOS electrolyte, the order increases from $r=0$ to $r=0.07$, however, the order decreases from $r=0.07$ to $r=0.45$. For 4SEOS electrolyte, the order decreases from $r=0$ to $r=0.17$. Further analysis is needed to understand the ionic liquid effect on the order-disorder transition of the block copolymer electrolytes. However, it is important to highlight that the ordered

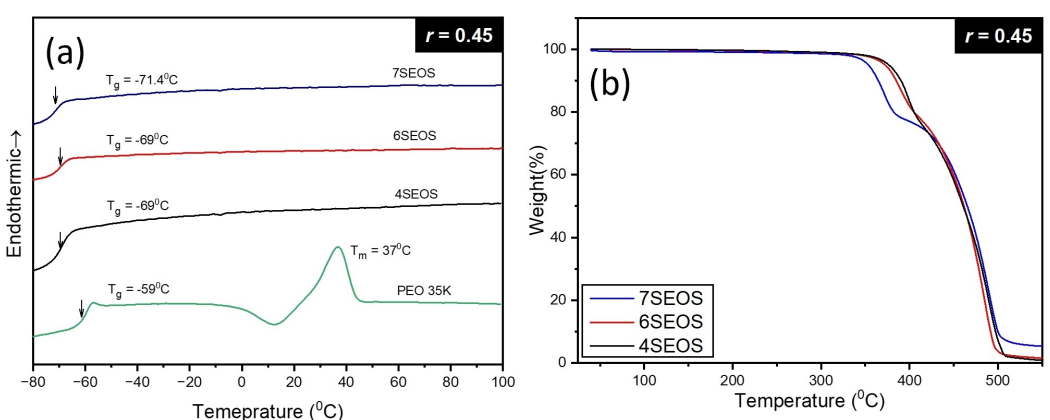


Figure 4. (a) DSC traces of PEO homopolymer and block copolymers at $r=0.45$, and (b) TGA thermograms of polymer membranes at $r=0.45$.

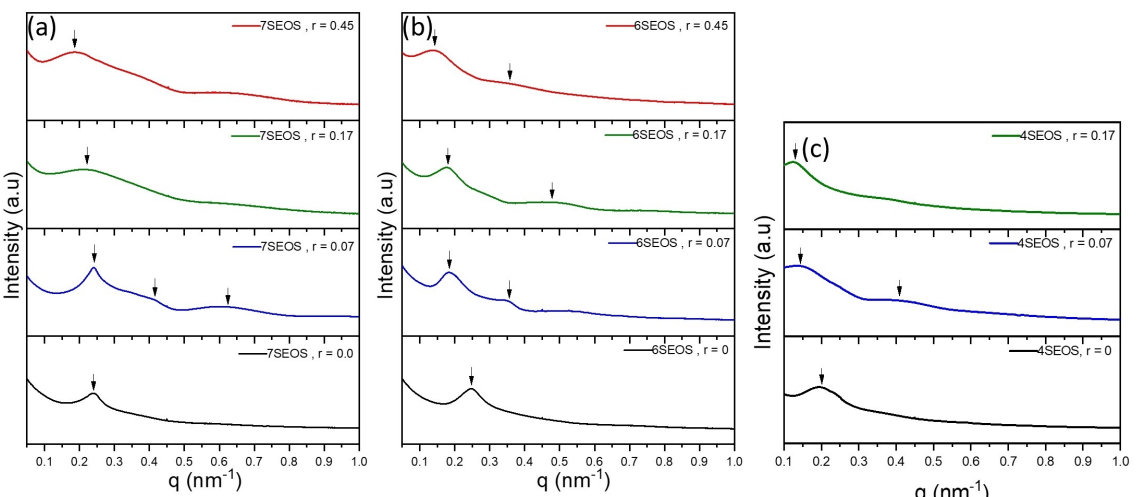


Figure 5. SAXS patterns of neat PS-*b*-PEO-*b*-PS block copolymers and of (a) 7SEOS, (b) 6SEOS and (c) 4SEOS electrolytes at different r values and at 25°C .

phases are present in all r values range, regardless of the block copolymer electrolyte (7SEOS, 6SEOS and 4SEOS).

Figure 6 shows dark-field STEM images of 7SEOS and 6SEOS electrolytes at $r=0.45$. The dark phase corresponds to the phase with lower electron density, i.e., PS is represented by the dark spots in both electrolytes. STEM images suggest short-range order with an inverted cylindrical phase. The cylindrical polystyrene phase is surrounded by a continuous conducting matrix (PEO and EMIMTFSI), due to a combination of packing frustration of the PS chains that arises from the strong selectivity of EMIMTFSI for the PEO block. STEM images confirm the microphase separation with the lack of long-range order observed by SAXS measurements. The formation of these kind of low ordered phases was previously reported in block copolymer/ionic liquid studies at high concentrations of ionic liquids.^[24,25]

Changes in domain spacing, d , obtained in microphase separated systems, are essential for understanding the degree of segregation for block copolymer/ionic liquid systems with increasing ionic liquid concentration. Addition of a selective solvent (ionic liquid in our case) to a block copolymer results in a drive to decrease the interfacial area, in order to reduce the

number of unfavourable contacts between the insoluble block and the solvent. This brings about increased chain stretching normal to the interface, and thus, an increase in the domain spacing. The characteristic domain spacing, d , is given by the Equation $d=2\pi/q^*$ and is plotted against r in Figure 7a. The data are derived from SAXS profiles. The addition of the EMIMTFSI ionic liquid results in an increase in domain spacing over the entire range of r values for each block copolymer electrolyte. These results are consistent with previous reported results.^[26] The highest domain spacing (50.7 nm) is for the 4SEOS block copolymer electrolyte at $r=0.17$, followed by 6SEOS and 7SEOS electrolytes (44.5 and 35.6 nm, respectively) at $r=0.45$. It is well established that domain spacing is governed by segregation strength, χN (where χ is the Flory-Huggins interaction parameter, and N is the copolymer chain length), and the volume fraction of the conducting phase, ϕ_c .^[27-29] An indication of the stretched nature of the PEO chains is the scaling of the domain spacing with the increase of N as shown in Figure 7b. The 4SEOS block copolymer electrolyte at $r=0.17$ presents the highest domain spacing (50.7 nm) at the highest N (554). We propose the increase of domain spacing upon ionic liquid-doping may be attributed to the copolymer chain length

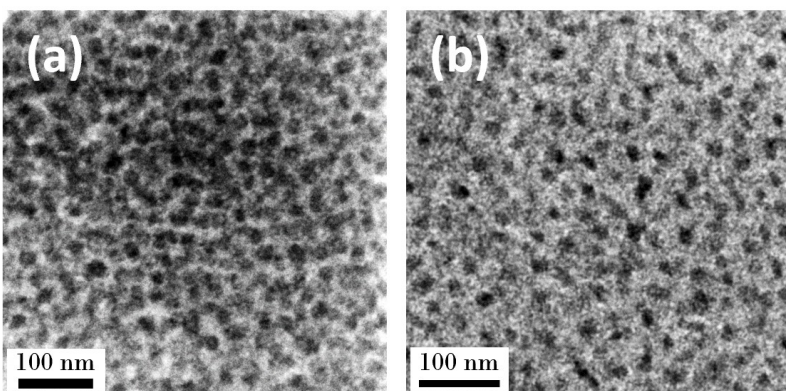


Figure 6. STEM images of (a) 6SEOS and (b) 7SEOS block copolymers at $r=0.45$.

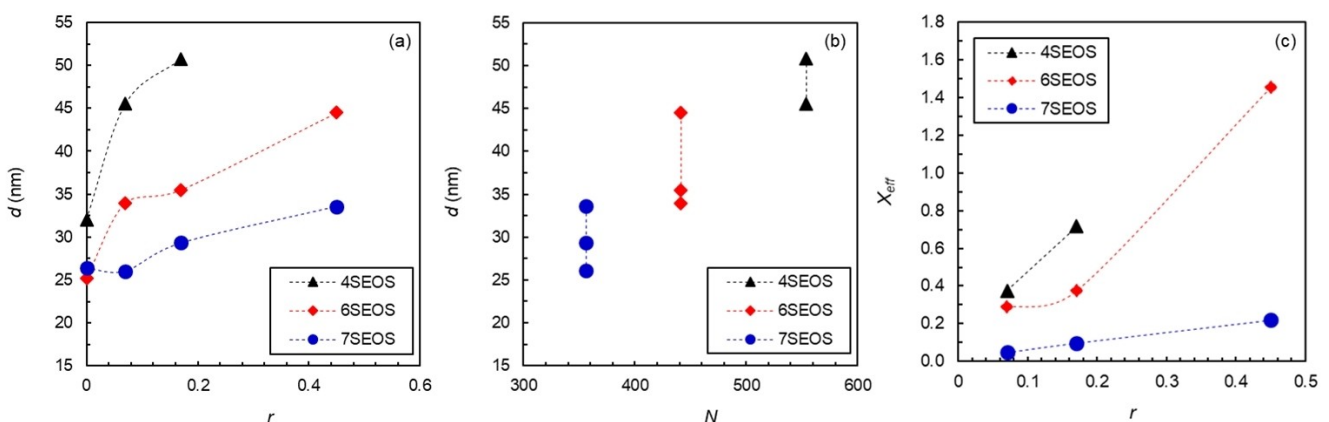


Figure 7. (a) The calculated domain spacing (d) as a function of r values, (b) domain spacing (d) vs chain length (N), and (c) the variation of interaction parameter (χ_{eff}) at different r values.

and the volume of ionic liquid added to the copolymer. In the strong segregation regime ($\chi N > 10$), the percentage of interfacial volume will become negligible, chain stretching will dominate, and the domain spacing is expected to scale as $d \sim \chi^{1/6}$.^[30] Figure 7c shows χ_{eff} (i.e. the polymer/ionic liquid interaction parameter) at different r values at 25 °C. χ_{eff} increases with the increase of the r values and also with the increase of N , and therefore, it suggests an increase in the effective interaction parameter between the structural PS block and the ionic liquid-containing PEO block. These results are in good agreement with the increase of χ_{eff} for blends of ionic liquids that are selective for one of the blocks.^[31] The product $\chi_{\text{eff}}N$ (which reflects the swelling and the polymer/ionic liquid interactions) in these block copolymer electrolytes is higher than 10 indicating that they are in the ordered regime. It is worth noting that 6SEOS at $r=0.45$ presents higher segregation strength than 7SEOS at $r=0.45$. However, further work is required to understand this behavior and establish the underpinnings of the dependence of the degree of segregation on the conductivity.

DMA measurement was performed on the 6SEOS block copolymer electrolyte at $r=0.45$. Figure 8 represents storage and loss modulus (G' and G'' , respectively) as a function of temperature. The block copolymer electrolyte is almost insensitive to G' and exhibits negligible changes in G'' ($G'' \ll G'$) over all temperature ranges, suggesting that the block copolymer electrolyte has a solid behaviour.

Symmetric Full Cell Cycling

The membrane of 6SEOS block copolymer at $r=0.45$ was used as a solid-state electrolyte in two symmetric full cell configurations, namely CNT|6SEOS_{0.45}|CNT and AC|6SEOS_{0.45}|AC using CNT mat and activated carbon electrodes, respectively. Prior to fabrication of the CNT based solid-state cells, the CNT mats were studied as anode and cathode and tested in liquid state full cells with neat EMIMTFSI, as shown in Figure S2a-c. A comparison of the cyclic voltammograms (CVs) of both solid

and liquid state cells is shown in Figure 9a. Both the liquid and solid-state cells have similar profiles and exhibit features typical of double layer capacitance behaviour. At a scan rate of 50 mV/s between 0.1 V to 3 V, the CNT mats exhibit an areal capacitance of 14 mF/cm² and 12 mF/cm² in liquid state and solid-state, respectively. Figure 9b represents the galvanostatic charge-discharge (GCD) curves of CNT|6SEOS_{0.45}|CNT cell at different current densities from 0.5 A/g to 4 A/g for evaluating the rate capability of the polymer electrolyte. The cell exhibits a specific capacitance (C_{sp}) 6.8 F/g at a current density of 0.5 A/g and maintains a capacitance of 6.8 F/g, 6.7 F/g and 6.1 F/g at current densities of 1 A/g, 2 A/g and 4 A/g, respectively. The IR drop is considered an important characteristic of supercapacitors as large voltage drops lead to a loss of energy density, and therefore a low IR drop is preferred for practical applications. At 0.5 A/g, the supercapacitor exhibits negligible IR drop of 0.02 V, while a drop of 0.13 V was observed at 4 A/g as shown in Figure 9b (inset). This higher rate capability and low IR drop can be attributed to the lower internal resistance the CNT mats. The long cycling stability of CNT|6SEOS_{0.45}|CNT symmetrical supercapacitor was tested at a current density of 4 A/g for 40000 cycles between 0.1 V and 3 V in 2023 coin-cells, as shown in Figure 9c. The electrodes maintain a capacity of 6 mAh/g for several thousand cycles and after 40000 cycles the measured capacity was 5.6 mAh/g, which is above 93% capacity retention. Throughout cycling, the cell maintained a coulombic efficiency above 99%. Overall, the symmetrical cell exhibits an energy density of 7.9 Wh/kg at a 1 A/g with a power density of 1.4 kW/kg. An energy density of 7.1 Wh/kg is observed at a higher current density of 4 A/g with a power density of over 5.6 kW/kg.

Figure 9c (inset figure) represents the Nyquist plots of the CNT|6SEOS_{0.45}|CNT cell before and after 2000 cycles. The high frequency region reveals a small semicircle followed by a steep slope at lower frequencies representing double layer capacitance (EDL). The intercept at the higher frequency, representative of the electrode resistance (R_e)^[32] was measured as 12.42 Ω. The mid frequency region corresponding to the electrolyte resistance, (R_s) was measured as 19.78 Ω initially and 16.75 Ω post 2000 cycles. Overall, the internal resistance shows a minimal change post cycling, indicating minimal cell degradation.

To evaluate the high temperature operational performance, the CNT|6SEOS_{0.45}|CNT cells were cycled at a current density of 4 A/g at 60 °C shown in Figure 10. The cell exhibits an initial capacity of 7.1 mAh/g and the capacity is seen to gradually increase past 5000 cycles and stabilises around 17000 cycles. We suggest that the capacity increase above 5000 cycles may be due to the gradual infiltration of the electrode by the electrolyte at higher temperature. The cell maintains a coulombic efficiency close to 100% during all cycling, a capacity of 7.3 mAh/g is observed at the end of 60000 cycles. Overall, the cell when cycled at 60 °C exhibits only a minor improvement in cycling characteristics over 25 °C. At 60 °C when cycled at a current density of 4 A/g the specific capacitance was measured as 6.4 F/g with energy and power densities of 10.3 Wh/kg and 5.8 kW/kg, respectively. The thin nature and

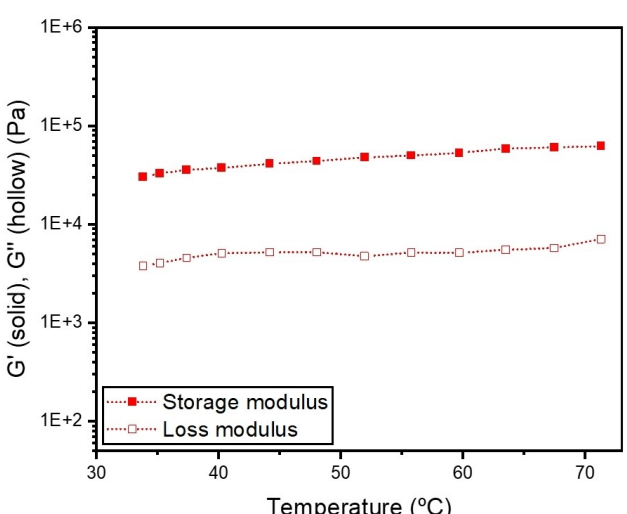


Figure 8. DMA analysis of membrane 6SEOS_{0.45}.

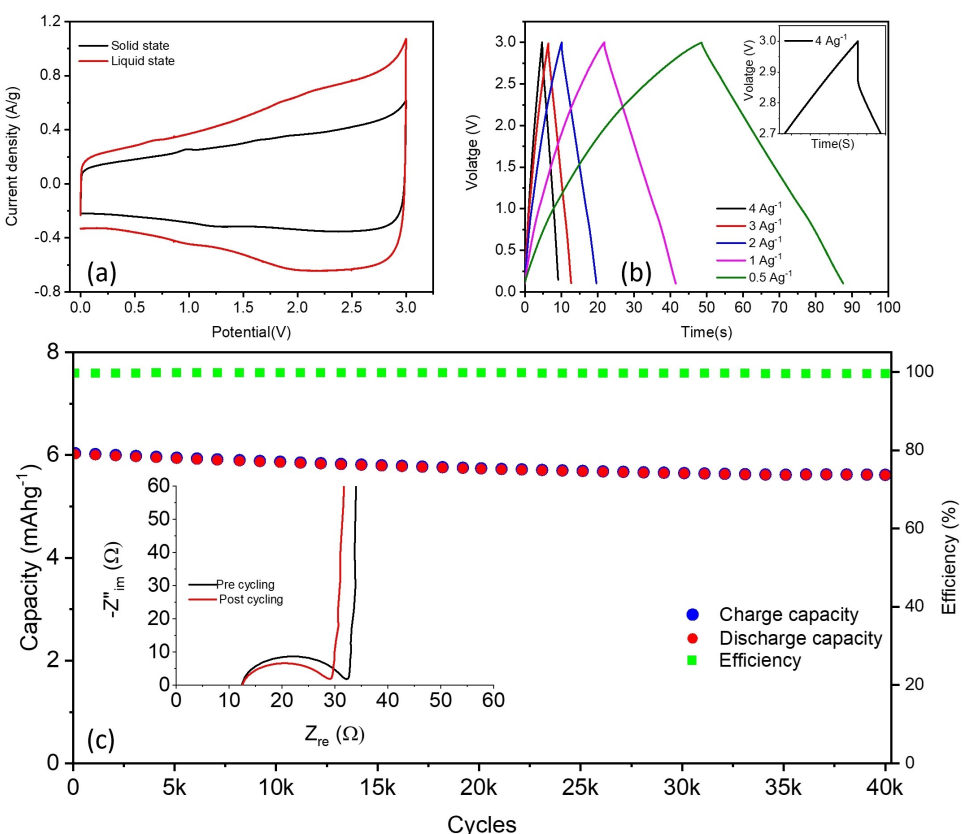


Figure 9. (a) Electrochemical characterisation of CNT|6SEOS_{r=0.45}|CNT symmetric cell, comparison of cycling voltammetry of liquid state cell vs solid state cell at 25 °C, (b) GCD curves at current densities from 0.5 A/g to 4 A/g (inset:- GCD curve at 4 A/g), and (c) galvanostatic cycling at 4 A/g for 40000 cycles (inset: EIS of symmetric cell post initial 2000 cycles) at 25 °C.

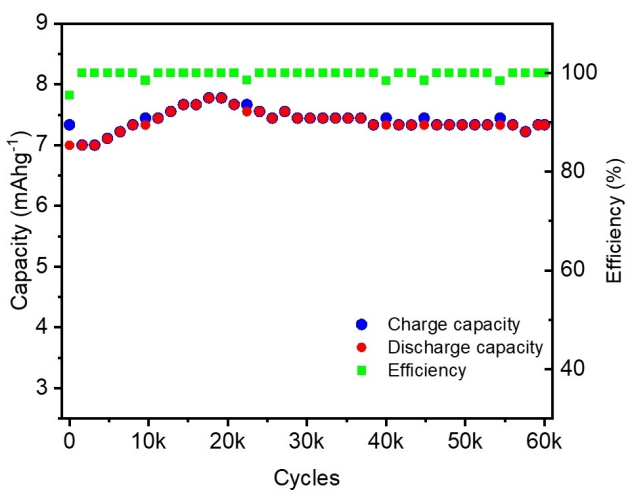


Figure 10. Galvanostatic cycling of CNT|6SEOS_{r=0.45}|CNT at 4 A/g at 60 °C.

excellent conductivity of the CNT mat leads to excellent material utilisation at both 25 °C and 60 °C.

To further test the compatibility of our electrolytes with different electrodes, electrodes based on activated carbon using 6SEOS electrolyte at $r=0.45$ as ion conducting binder were fabricated. Figure 11b represents the GCD curves of symmetric AC|6SEOS_{r=0.45}|AC full cells based on such electrodes. At 25 °C, the cell exhibits a capacity of 10 mAh/g at a current density of

1 A/g, which decreases to 6.6 mAh/g and 2.9 mAh/g at 2 A/g and 4 A/g, respectively, as shown in Figure 11a. The IR losses presented by AC|6SEOS_{r=0.45}|AC is much higher than CNT|6SEOS_{r=0.45}|CNT at all current densities and might be due to sluggish ion diffusion in the electrode due to a higher tortuosity.^[33,34] However, the cell maintains columbic efficiency close to 100% at all current densities.

Figure 11d represents GCD curves of AC|6SEOS_{r=0.45}|AC at 60 °C, the cell presents a capacity of 20 mAh/g at 1 A/g, which is double the capacity at 25 °C. Capacities of 17.3 mAh/g and 13.5 mAh/g are achieved at current densities of 2 A/g and 4 A/g, respectively (Figure 11c). This is significantly higher in comparison to the values at 25 °C. Furthermore, a significantly lower IR drop with higher specific capacity is observed at 60 °C, this can be attributed to the higher ionic conductivity of the block copolymer electrolyte and electrode at 60 °C.

To compare the performance of our solid-state supercapacitors, both AC and CNT devices, with commercial state-of-the-art supercapacitors (based on liquid-state electrolytes), the corresponding specific energy and power densities are shown in the Ragone plot (Figure 12). The energy density of symmetrical cells with AC decreases with the increase of the current densities (from 1 A/g to 4 A/g), being 20.7 Wh/kg (at 4 A/g) at 60 °C. This value is significantly higher than CNT|6SEOS_{r=0.45}|CNT (10.3 Wh/Kg at 4 A/g at 60 °C). At 25 °C, the energy density drops to 7.0 Wh/kg (at 4 A/g) for AC|6SEOS_{r=0.45}|AC and to

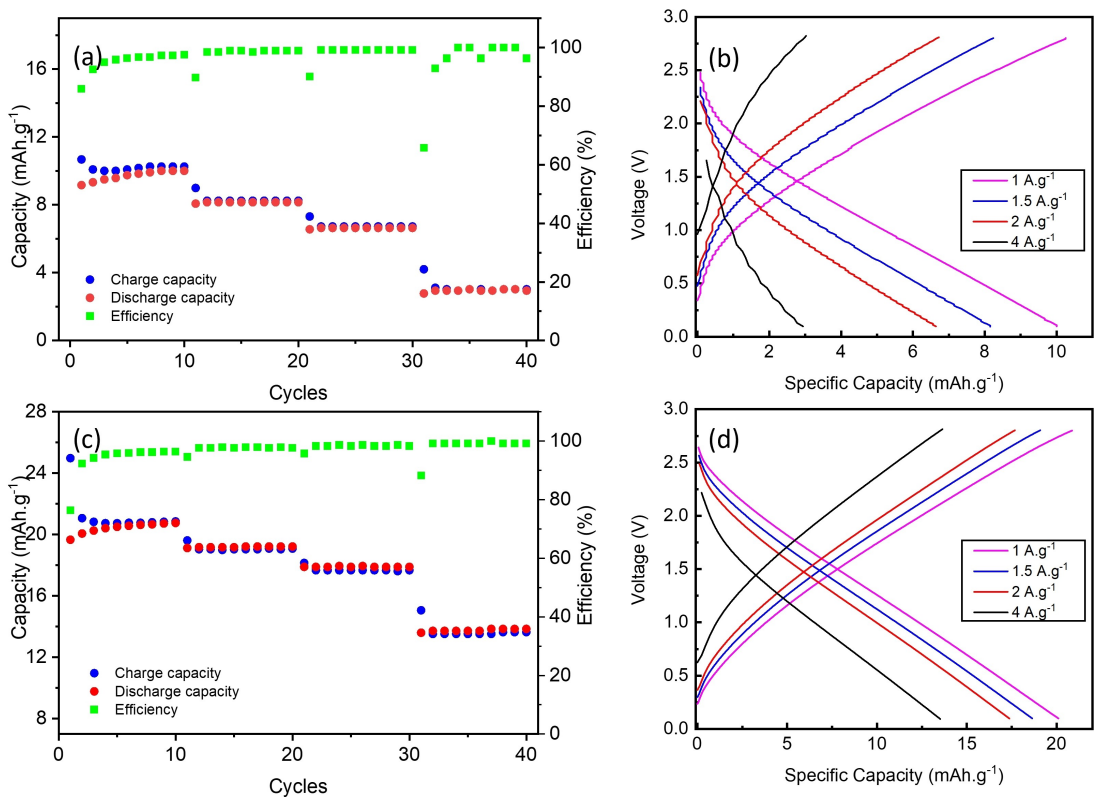


Figure 11. Electrochemical characterisation of (a & b) $\text{AC}|\text{6SEOS}_{\text{r}0.45}|\text{AC}$ symmetric cells at 25°C , (c & d) $\text{AC}|\text{6SEOS}_{\text{r}0.45}|\text{AC}$ symmetric cells at 60°C .

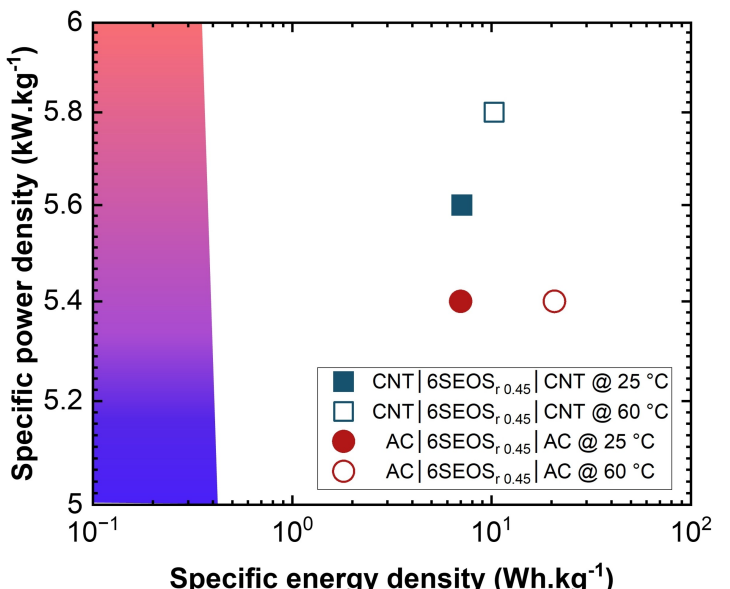


Figure 12. Ragone plot for $\text{AC}|\text{6SEOS}_{\text{r}0.45}|\text{AC}$ cells and $\text{CNT}|\text{6SEOS}_{\text{r}0.45}|\text{CNT}$ at 4 A/g and at 25°C and 60°C . The colour area shows the performance region of commercial state-of-art supercapacitors.^[35]

7.1 Wh/kg (at 4 A/g) for $\text{CNT}|\text{6SEOS}_{\text{r}0.45}|\text{CNT}$. The power density of AC based devices is 5.4 kW/kg at 4 A/g at both 25 and 60°C , which is similar to the values in CNT devices (5.6 and 5.8 kW/kg at 4 A/g at 25 and 60°C , respectively). The power density presented by AC electrode-based cells are superior to other published solid-state supercapacitors. For example,

1.3 kW/kg and 19 Wh/kg ($\text{AC/BCE}(\text{SiO}_2\text{-BC-BT})/\text{AC}$),^[35] 1.1 kW/kg and 16 Wh/kg ($\text{AC/PEGMA-PEGDMA-P}_{13}\text{FSI}/\text{AC}$),^[17] 0.2 kW/kg and 5.2 Wh/kg (AC/Chitosan/AC),^[36] and 0.0023 kW/kg and 21 Wh/kg (AC/CLPE/AC).^[17] The reports on CNT based solid-state are scarce, and the performance of our devices are comparable with the literature, for example Song *et al.*^[37] reported an energy

and power density of 3.5 Wh/kg and 28.1 kW/kg and Mapleback *et al.*^[23] reported 18.3 Wh/kg and 0.15 kW/kg using similar CNT mats but in liquid state.

At both temperatures, the CNT|6SEOS_{r=0.45}|CNT devices deliver higher power densities than that of the AC|6SEOS_{r=0.45}|AC, which is in agreement with the IR drop data. Overall, both solid-state AC|6SEOS_{r=0.45}|AC and CNT|6SEOS_{r=0.45}|CNT devices display better performance, in terms of both specific energy and power densities, than that of the commercial state-of-the-art capacitor, based on liquid electrolyte.

Conclusions

We investigated block copolymer electrolytes based on PS-*b*-PEO-*b*-PS and EMIMTFSI ionic liquid and their use as solid electrolytes for supercapacitors. At the highest *r* value (*r*=0.45), all the block copolymer electrolytes achieve conductivities above 10⁻⁴ S/cm at 25 °C due to lower T_g and increased polymer chain segmental motion. SAXS and STEM indicate a phase separated morphology with a lack of long-range ordering. Our results indicate that the domain spacing in the membranes is influenced by both the volume fraction of ionic liquid and the copolymer chain length (*N*). The interaction parameter (χ_{eff}) between the PS phase and ionic liquid bearing PEO phase increases with copolymer chain length and the *r* value. The best performing block copolymer electrolyte (6SEOS at *r*=0.45) in terms of ionic conductivity and mechanical properties was selected for testing in two different configurations based on CNT mats and activated carbon electrodes. Structural devices based on CNT mats owing to their lower internal resistance were shown to have superior rate capability with minimum IR drop at higher current densities. Activated carbon based cells exhibited higher capacity in comparison to CNT based devices owing to higher surface area. While activated carbon based devices are suited for energy dense applications, for high power applications CNTs shine due to their superior rate capability. Overall, nanostructured ionic liquid containing block copolymer electrolytes exhibit excellent performance demonstrating its viability in supercapacitor applications.

Acknowledgements

The authors acknowledge the financial support of Basque Government through CICe-2022 ELKARTEK (KK-2022/00043), CICe-2023 ELKARTEK (KK-2023/00063), and through the Australian Research Council via the ARC Industry Transformation Training Centre for Future Energy Technologies (storEnergy, IC180100049). We also gratefully acknowledge the ALBA synchrotron facility (Proposal number 2021024913) for the funding and help to perform the SAXS experiments at BL11-NCD-SWEET beamline with the collaboration of ALBA staff. The authors would like to thank Prof. Nitash P. Balsara for the helpful discussion and suggestions regarding to SAXS analysis.

Conflict of Interests

The authors declare no conflict of interest.

Data Availability Statement

Data sharing is not applicable to this article as no new data were created or analyzed in this study.

Keywords: Solid-state electrolyte • Block copolymer • Ionic liquids • Supercapacitor

- [1] Y Wang, L Zhang, H Hou, et al., *J. Mater. Sci.* 2020, 56(1), 173–200. DOI: 10.1007/S10853-020-05157-6.
- [2] J Libich, J Máca, J Vondrák, O Čech, M. Sedlářková, *J. Energy Storage.* 2018, 17, 224–227. DOI: 10.1016/J.EEST.2018.03.012.
- [3] V. V. N. Obreja, *Phys. E Low Dimens. Syst. Nanostruct.* 2008, 40(7), 2596–2605. DOI: 10.1016/J.PHYSCE.2007.09.044.
- [4] T. P. Mofokeng, Z. N. Tetana, K. I. Ozoemena, *Carbon N Y.* 2020, 169, 312–326. DOI: 10.1016/J.CARBON.2020.07.049.
- [5] Z. Yang, J. Tian, Z. Yin, C. Cui, W. Qian, F. Wei, *Carbon N Y.* 2019, 141, 467–480. DOI: 10.1016/J.CARBON.2018.10.010.
- [6] K. Komatsubara, H. Suzuki, H. Inoue, et al., *ACS Appl. Nano Mater.* 2022, 5(1). DOI: 10.1021/acsanm.1c04236.
- [7] R. Taslim, A. Apriwandi, E. Taer, *ACS Omega* 2022, 7(41). DOI: 10.1021/acsomega.2c04301.
- [8] Y. Zhang, C. Wu, S. Dai, et al., *J Colloid Interface Sci.* 2022, 606. DOI: 10.1016/j.jcis.2021.08.042.
- [9] K. Aruchamy, K. Dharmalingam, C. W. Lee, D. Mondal, N. S. Kotrappanavar, *Chem. Eng. J.* 2022, 427. DOI: 10.1016/j.cej.2021.131477.
- [10] T. Tsubota, M. Morita, S. Kamimura, T. Ohno, *J. Porous Mater.* 2016, 23(2), 10. DOI: 10.1007/s10934-015-0087-6.
- [11] A. M Sampaio, G. F. L. Pereira, M. Salanne, L. J. A. Siqueira, *Electrochim Acta.* 2020, 364, 137181. DOI: 10.1016/J.ELECTACTA.2020.137181.
- [12] S. K Singh, A. W. Savoy, *J Mol Liq.* 2020, 297, 112038. DOI: 10.1016/J.MOLLIQ.2019.112038.
- [13] A. M Soomro, B. Jawed, J. B. Soomro, et al., *Electronics (Switzerland).* 2022, 11(18), 2903. DOI: 10.3390/ELECTRONICS11182903/S1.
- [14] X. Yang, F. Zhang, L. Zhang, T. Zhang, Y. Huang, Y. Chen, *Adv. Funct. Mater.* 2013, 23(26), 3353–3360. DOI: 10.1002/ADFM.201203556.
- [15] P. Pal, A. Ghosh, *Electrochim Acta.* 2018, 278, 137–148. DOI: 10.1016/J.ELECTACTA.2018.05.025.
- [16] C. Ramasamy, P. Porion, L. Timperman, M. Anouti, *Synth. Met.* 2023, 299. DOI: 10.1016/j.synthmet.2023.117469.
- [17] V. Chaudoy, F. T. Van, M. Deschamps, F. Ghamouss, *J. Power Sources* 2017, 342. DOI: 10.1016/j.jpowsour.2016.12.097.
- [18] C. Novakov, R. Kalinova, S. Veleva, F. Ublekov, I. Dimitrov, A. Stoyanova, *Gels* 2023, 9(4). DOI: 10.3390/gels9040338.
- [19] I. Villaluenga, X. C. Chen, D. Devaux, D. T. Hallinan, N. P. Balsara, *Macromolecules.* 2015, 48(2), 358–364. DOI: 10.1021/MA502234Y/ASSET/IMAGES/LARGE/MA-2014-02234Y_0003.JPG.
- [20] L. Porcarelli, M. A. Aboudzadeh, L. Rubatat, et al., *JPS.* 2017, 364, 191–199. DOI: 10.1016/J.JPOWSOUR.2017.08.023.
- [21] D. de M. Zanata, M. I. Felisberti, *Eur Polym J.* 2022, 167. DOI: 10.1016/J.EURPOLYMJ.2022.111069.
- [22] G. K Sethi, H. Y Jung, W. S Loo, et al., *Macromolecules.* 2019, 52(9), 3165–3175. DOI: 10.1021/ACS.MACROMOL.9B00042/ASSET/IMAGES/MEDIUM/MA-2019-00042Q_M034.GIF.
- [23] B. J Mapleback, T. J. Simons, Y. Shekibi, K. Ghorbani, *Electrochim Acta.* 2020, 331. DOI: 10.1016/j.electacta.2019.135233.
- [24] M. L Hoarfrost, R. A. Segelman, *ACS Macro Lett.* 2012, 1(8). DOI: 10.1021/mz300241g.
- [25] L. Gwee, J. H. Choi, K. I. Winey, Y. A. Elabd, *Polymer (Guildf).* 2010, 51(23) DOI: 10.1016/j.polymer.2010.09.026.
- [26] C. Lai, W. B Russel, R. A. Register, *Macromolecules.* 2002, 35(10). DOI: 10.1021/ma0122223.
- [27] W. S Loo, N. P. Balsara, *J. Polym. Sci. B Polym. Phys.* 2019, 57(18). DOI: 10.1002/polb.24800.

- [28] Y. Ren, T. P. Lodge, M. A. Hillmyer, *Macromolecules*. **2002**, *35*(10). DOI: 10.1021/ma011958x.
- [29] xGu, I. Gunkel, A. Hexemer, T. P. Russell, *Macromolecules*. **2016**, *49*(9). DOI: 10.1021/acs.macromol.6b00429.
- [30] T. M. Bennett, K. S. Jack, K. J. Thurecht, I. Blakey, *Macromolecules*. **2016**, *49*(1). DOI: 10.1021/acs.macromol.5b02041.
- [31] J. Y. Wang, W. Chen, T. P. Russell, *Macromolecules*. **2008**, *41*(13). DOI: 10.1021/ma800718z.
- [32] B. A. Mei, O. Munteşari, J. Lau, B. Dunn, L. Pilon, *J. Phys. Chem. C* **2018**, *122*(1), 194–206. DOI: 10.1021/ACS.JPCC.7B10582/ASSET/IMAGES/LARGE/JP-2017-10582X_0009.JPG.
- [33] X. Wu, S. Zheng, Y. Huang, et al. *J. Power Sources* **2021**, *482*. DOI: 10.1016/j.jpowsour.2020.228996.
- [34] W. Yang, W. Yang, F. Ding, L. Sang, Z. Ma, G. Shao, *J. Power Sources*. **2021**, *482*. DOI: 10.1016/j.jpowsour.2020.228996.
- [35] P. L. Handayani, L. Nulandaya, J. Y. Cheon, T. Kim, S. I. Yoo, U. H. Choi, *Chem. Eng. J.* **2022**, *429*, 132273. DOI: 10.1016/J.CEJ.2021.132273.
- [36] H. Yang, Y. Liu, L. Kong, L. Kang, F. Ran, *J. Power Sources* **2019**, *426*. DOI: doi:10.1016/j.jpowsour.2019.04.023.
- [37] L. Song, X. Cao, L. Li, et al., *Adv. Funct. Mater.* **2017**, *27*(21). DOI: 10.1002/adfm.201700474.

Manuscript received: September 9, 2024

Revised manuscript received: November 12, 2024

Version of record online: December 4, 2024